ADVANCED FUNCTIONAL MATERIALS
www.afm-journal.de

4D Printed Cardiac Occlusion Device with Efficient Anticoagulation, Proendothelialization, and Precise Localization

Mengjiao Yang, Yingjie Xu, Xiaozhou Xin, Chengjun Zeng, Yuanshi Li, Cheng Lin, Yanju Liu,* Yuanyuan Guo,* and Jinsong Leng*

Congenital heart defects (CHDs) are one of the most common congenital malformations, accounting for ≈30% of all congenital malformations. Interventional implantation of occlusion devices is becoming the preferred treatment for CHDs. However, current occlusion devices suffer from serious problems, such as thrombosis, slow endothelialization, imprecise localization, abrasion, displacement, etc. Here, a multifunctional drug-carrying fiber platform with structural similar to the extracellular matrix is innovatively designed to develop 4D printed cardiac occlusion devices, with characteristics of efficient anticoagulation, proendothelialization, and precise localization. Biomimetic ligament structures are designed to achieve a similar mechanical response to myocardial tissue, which helps to synergize deformation and reduce tissue wear. A structural design method for biomimetic personalized multilevel occlusion devices is proposed, facilitating further improvement of sealing reliability. The radiopaque 4D printed shape memory composites are developed, realizing the complete visualization and precise localization of the device in vivo. The novel 4D printed cardiac occlusion device provides an effective way to reduce the risk of complications and contributes to versatility. It is expected to be a next-generation multifunctional repair device for personalized treatment of CHDs.

1. Introduction

Congenital heart defects (CHDs) are anatomical abnormalities caused by impaired formation or abnormal development of the heart and large blood vessels during embryonic development. It is estimated that there are 8 CHDs per 1000 births.[1,2] CHD is a critical cause of neonatal deaths globally, which may lead to a series of severe complications, such as heart failure if left untreated. Ventricular septal defect (VSD) is an abnormality of blood flow from left to right at the level of the ventricles, with 4 out of 10 CHD patients being VSD patients.[3,4] Although the traditional gold standard intervention for VSD treatment has been open-heart surgery, cardiac occlusion devices are increasingly being used to close VSDs due to their encouraging efficacy. VSD occlusion devices essentially serve as a temporary platform for autologous tissue adhesion, and when the defect is covered by intact and firm autologous tissue (the process known as endothelialization), the device ideally disappears with the completion of the endothelialization process.

However, most current occlusion devices are composed of Ni-Ti alloy mesh and nonabsorbable occlusive membranes. These devices are able to block abnormal blood exchange, but can also cause serious complications.[2,5] For example, alloy-based device leads to nickel allergy and corrosion; large differences in stiffness and deformation between the occlusion device and cardiac tissue trigger abrasion; dimensional mismatch leads to misalignment and even embolization. In addition, there are problems, such as delayed endothelialization, thrombosis, and poor localization due to limited radiopaque points. The development of bioabsorbable occlusion devices eliminates the risk of complications such as nickel allergy and erosion.[5] For example, the BioTrek occluder developed by NMT Medical was a completely bioresorbable occlusion device.[3] BioTrek was made from P4HB and its degradation products can be excreted by the body. In addition, researchers have developed the Double Umbrella (DU) occlusion device, a fully bioresorbable device made from polycaprolactone (PCL) and polylactic acid-*co*-E-caprolactone (PLC).[6] However, these devices still suffer from monofunctionality, susceptibility to thrombus

M. Yang, C. Lin, J. Leng
Centre for Composite Materials and Structures
Harbin Institute of Technology
Harbin 150080, China
E-mail: lincheng@hit.edu.cn
Y. Xu, Y. Guo
Department of Cardiology, Department of Geriatrics
the First Affiliated Hospital of Harbin Medical University
Harbin 150001, China
E-mail: guoyuanyuan@hrbmu.edu.cn
X. Xin, C. Zeng, Y. Liu
Department of Astronautical Science and Mechanics
Harbin Institute of Technology
Harbin 150001, China
E-mail: yj_liu@hit.edu.cn
Y. Li
Department of Cardiology
Ningbo No. 2 Hospital
Ningbo 315000, China

The ORCID identification number(s) for the author(s) of this article can be found under https://doi.org/10.1002/adfm.202412533

DOI: 10.1002/adfm.202412533

formation, slow endothelialization, and imprecise localization. Moreover, these devices are still prepared using traditional manufacturing techniques, such as braiding. The complex anatomy of the cardiac defect site and the nonpersonalized device configuration increase the risk of complications such as abrasion, displacement, and embolism. Therefore, the development of 4D printed cardiac occlusion devices that are effective in anticoagulation, promotion of endothelialization, and precise localization is highly desired.

In response to the demand for personalized treatment of patients, 3D printing technology, a rapid prototyping technology that can manufacture arbitrary geometric shapes with high precision, has developed rapidly in the biomedical field at an astonishing rate.[7–9] However, the 3D printing structure is limited by the flaws of the fixed shape and performance after printing, thus the 4D printing technology came into being. 4D printing adds an extra dimension of "time" to 3D printing, breaking through the limitation that 3D printing cannot actively control the performance of the printed structure, and realizing the programmable transformation of its shape and function.[10–18] Combining intelligent materials with 3D printing is the way to achieve 4D printing. Shape memory polymers (SMPs) are intelligent materials capable of responding to external excitations by actively deforming to a desired temporary configuration and then recovering to the initial configuration. 4D printed SMPs show great potential for application in various types of implantable stents, drug release devices, and cardiac patches due to their programmable reconfigurability and adaptive deployment capability. The combination of 4D printing and SMPs offers the possibility of customizing complex structures and minimally invasive procedures, and the deployment of 4D printed SMP structures can adaptively match defect contours to improve surgical success rates.[14–16,19,20]

Herein, based on the 4D printed SMPs, novel next-generation bioabsorbable 4D printed cardiac occlusion devices were developed, with proendothelialization, anticoagulant, precise localization, and personalized customization characteristics (**Figure 1**). The cardiac occlusion device consisted of a 4D printed personalized biomimetic structure and a multifunctional drug-carrying fiber platform (MFDFP). As an important part of the occlusion device, whether it is the traditional alloy occlusion devices or the polymer occlusion devices, the occlusive membranes are just simple polymer films, even nonbioabsorbable, ignoring the importance of performing their function. Therefore, bioabsorbable MFDFP with a fibrous structure similar to the microstructure of the extracellular matrix was innovatively developed to replace conventional occlusive membranes and help promote cell adhesion and proliferation. In addition, anticoagulant and endothelialization-promoting drug components were introduced into MFDFP, providing an effective way to address the challenges of thrombosis and slow endothelialization. Radiopaque 4D printed shape memory composites were developed and used as raw materials to prepare personalized occlusion devices through 4D printing. This allowed the homogeneous radiopacity of the occlusion device for precise localization and contributed to the success rate of the blockage due to the active self-matching deformation capability. Biomimetic metamaterial structure with a similar stress–strain response to biological tissue was introduced into the structural design of the personalized occlusion device, which was conducive to achieving cooperative deformation with cardiac tissue and reducing the risk of abrasion, perforation, etc.[21,22] The mechanical performance, programmable reconfigurability, biocompatibility, and radiopacity of 4D printed cardiac occlusion devices were systematically evaluated, and the excellent anticoagulant and proendothelialization properties of the MFDFP were verified. The 4D printed devices solved the problems of allergy and corrosion caused by traditional alloy occlusion devices and compensated for the problems of delayed endothelialization, thrombosis, imprecise localization, and displacement of the current bioabsorbable occlusion devices. It is predicted that they are expected to become the next generation of multifunctional personalized occlusion devices.

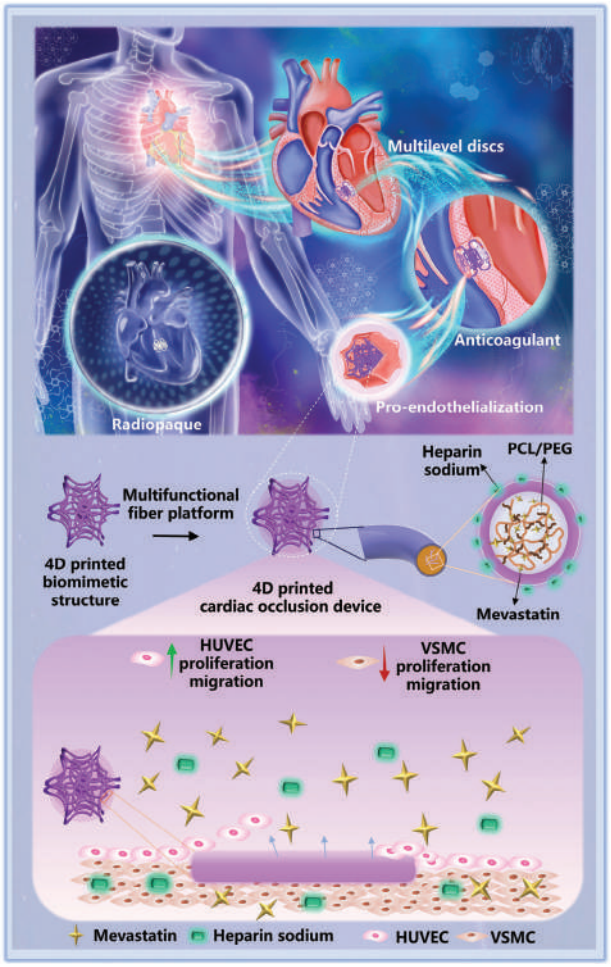

Figure 1. 4D printed cardiac occlusion device with highly efficient anticoagulation, proendothelialization, and precise localization.

2. Results and Discussions

2.1. Preparation and Characterization of MFDFP

Electrospinning fiber membrane has a structure similar to the extracellular matrix,[23,24] thus MFDFP was constructed using electrospinning technology to promote cell adhesion, growth, and accelerate endothelialization, providing a temporary and effective platform for self-recovery of cardiac tissues. PCL is

a biomaterial with good biocompatibility and biodegradability, but its inherent hydrophobicity is not conducive to cell adhesion.[25] Therefore, the hydrophilic polymer polyethylene glycol (PEG) was used to modify PCL to enhance cell adhesion and proliferation properties. In addition, to inhibit thrombosis and improve vascular endothelial function, heparin sodium as well as the ester lipophilic statin mevastatin were introduced (Figure 1), which have excellent anticoagulant and nitric oxide synthesis-promoting properties, respectively. **Figure 2**a illustrates the preparation process of MFDFP, mevastatin, and heparin sodium were compounded with PEG/PCL to build the MFDFP with extracellular matrix-like microstructure, anticoagulant, and endothelial-promoting properties by electrospinning technology. MFDFP exhibited a uniform fiber morphology (Figure 2a; and Figure S1, Supporting Information), and the fibers were interstacked to form a 3D network structure, which helped to promote cell adhesion and growth. The MFDFP without heparin sodium and mevastatin was abbreviated as 0%MFDFP, the MFDFP with 2% heparin sodium was abbreviated as 2%Hs-MFDFP, the MFDFP with 4% heparin sodium and 2% mevastatin was abbreviated as 4%Hs/2%Me-MFDFP, and so on. The characteristic peaks in MFDFP were analyzed using Fourier transform infrared (FTIR) spectroscopy. Characteristic absorption peaks were observed at 2950 and 1730 cm^{-1}, attributed to stretching vibrations of —CH_2 and C═O in PCL. For 2%Hs/4%Me-MFDFP, there was a typical C═O characteristic peak (3500 cm^{-1}), demonstrating the successful loading of mevastatin (Figure 2b2). The effect of heparin sodium and mevastatin on the crystallinity of MFDFP was investigated by X-ray Diffraction (XRD) tests. The characteristic diffraction peaks of the (110) and (200) crystal planes in PCL can be clearly observed at 2θ = 21.3° and 24.3° (Figure 2c). The XRD patterns of 0%MFDFP and 2%Me-MFDFP showed that the (110) crystal plane diffraction peaks were significantly higher and sharper after loading of mevastatin, which may be attributed to the increase in crystallinity of MFDFP due to the addition of mevastatin. On the contrary, the diffraction peak intensity of the (110) crystal plane of the XRD pattern of 2%Hs-MFDFP slightly decreased after the addition of heparin sodium, which may be caused by the grain thinning of PCL in MFDFP after loading heparin sodium. The XRD results were also further verified by the mechanical test results of MFDFP (Figure S2, Supporting Information). The 2%Me-MFDFP exhibited the strongest diffraction peak and also the highest strength, with a tensile strength of nearly 700 kPa. The diffraction peak of PCL in 4%Hs/2%Me-MFDFP was slightly lower than that of 2%Me-MFDFP, and its tensile strength was second only to that of 2%Me-MFDFP, ≈600 kPa. The chemical elements of MFDFP were analyzed using an X-ray photoelectron spectrum (XPS). The spectra of 2%Hs/4%Me-MFDFP and 4%Hs/2%Me-MFDFP exhibited additional characteristic peaks of S2p and N1s that were not present in 0%MFDFP at 169 and 399 eV, respectively (Figure 2d–h; and Figures S3–S5, Supporting Information). With the increase of heparin sodium content, the diffraction peak intensities of S2p and N1s were enhanced, confirming that heparin sodium was successfully loaded into the MFDFP (Figure 2f,g).

2.2. Design and Characterization of the Biomimetic Ligament Structure (BLS)

Differences in mechanical performance between occlusion devices and biological tissues may lead to abrasion, erosion, and even perforation. The wavy BLS was capable of achieving a "J" shaped mechanical response resembling that of the tissue and achieving synergistic deformation with the myocardial tissue,[21,22,26,27] thus BLS was introduced in the occlusion device to avoid myocardial tissue abrasion. Six wavy BLSs with rotational symmetry were designed, and their mechanical performance was adjusted by designing structural geometric parameters (**Figure 3**a). The geometric parameters of the BLSs included α, θ, L/l, θ/L, w/l, d/l, and α/l. α was the ligament angle, θ was the central angle corresponding to the arcuate and crescentic ligaments. L was the linear length of the ligaments, and w was the ligament thickness. l was the distance between the ends of the ligaments, and d was the diameter of the node. The detailed design geometric parameters of the BLSs are shown in Table S1 (Supporting Information). The BLSs were accurately prepared by 4D printing, and the structures, such as nodes and ligaments were clearly visualized (Figure 3b).

With the introduction of the radiopaque filler barium sulfate ($BaSO_4$) into the bioabsorbable PEG/poly (lactic acid) (PLA) composites, 4D printed radiopaque filaments were successfully prepared and used for printing BLS/occlusion devices to realize uniform radiopacity and precise localization (Figures S6 and S7, Supporting Information). The mechanical performance of the BLSs was analyzed. BLSs showed a "J"-shaped stress–strain curve similar to that of biological tissues when subjected to uniaxial tensile loading (Figure 3c), which was attributed to the fact that the BLS underwent a nonlinear deformation process consisting of the following three stages. In the first stage, the BLS was in a bending-dominated deformation mode, and the closely arranged bent ligaments were gradually straightened under tensile loading. At this stage, the bent ligaments were subjected to smaller stresses to produce larger strain, and thus the structural equivalent stiffness of the BLS was at a low level. As the strain continued to increase, the modulus slowly rose (the second stage). The deformation mode of the BLS gradually transitioned from bending-dominated to tensile-dominated, and the modulus rose slowly. When the strain of BLS exceeded the critical strain, the deformation mode changed to tensile dominance, resulting in a sharp increase in the modulus and a rapid increase in the structural equivalent stiffness (the third stage). BLS2 and BLS3 exhibited similar moduli, and the elongation at break of both was ≈80%–100%. Compared to other BLS, the elongation at break of BLS1 exceeded 170%, which may be attributed to the higher degree of ligament bending in BLS1, resulting in elevated critical deformation. BLS4 and BLS5 had slightly lower elongation at break due to the small degree of ligament bending, while BLS6 had obviously higher elongation at break due to the introduction of nodes. This was due to the fact that the nodes provided more cushioning for the bending deformation of the BLS, and the nodes produced rotational deformation with the ligaments during load bearing, thus increasing the critical deformation for the transition from bending dominance to tensile dominance. In addition, the

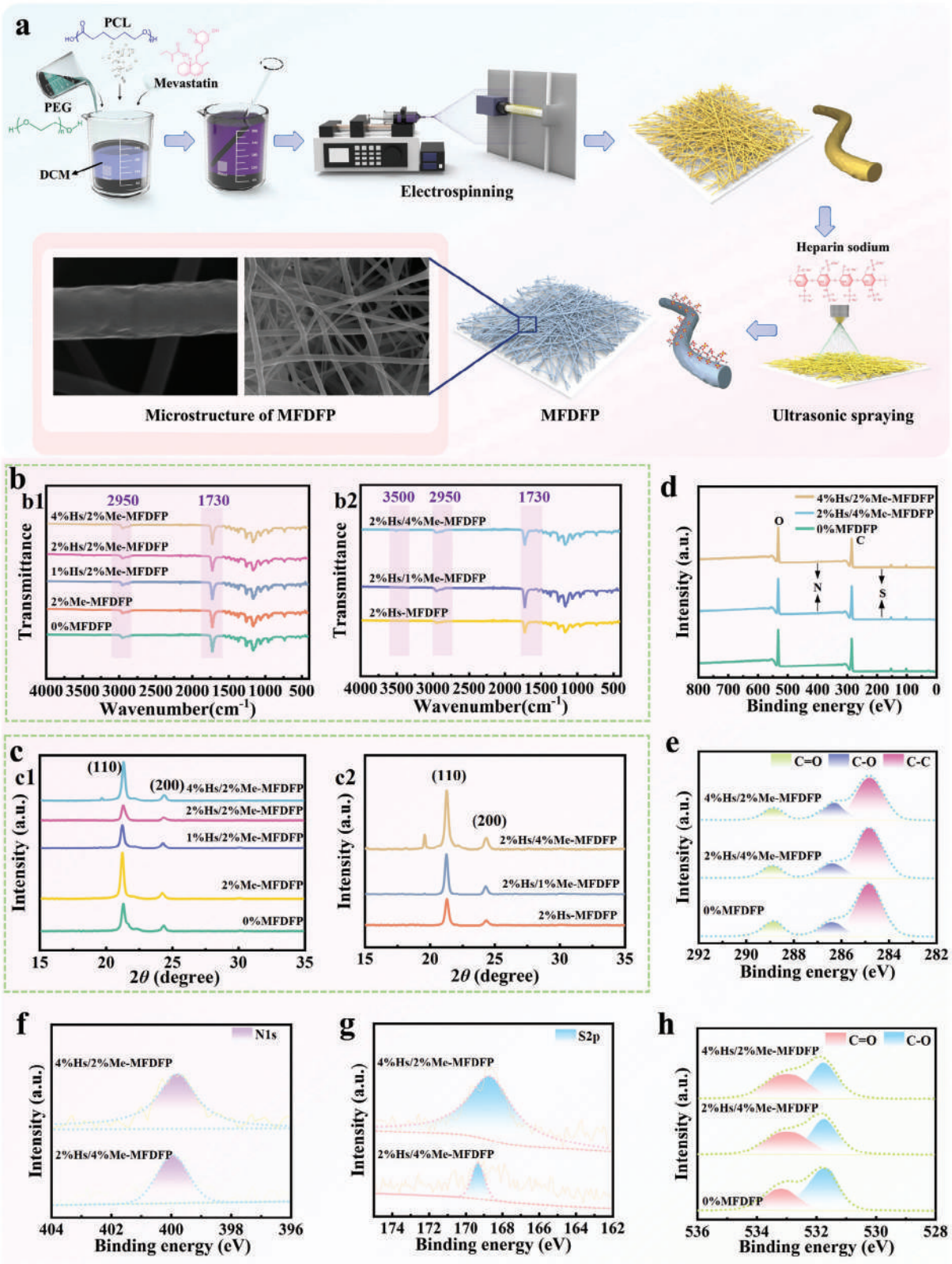

Figure 2. a) Schematic preparation of MFDFP and morphological characterization of MFDFP. b–g) Characterization of MFDFP. b) FTIR curves. b1) FTIR curves of MFDFP containing different concentrations of heparin sodium. b2) FTIR curves of MFDFP containing different concentrations of mevastatin. c) XRD patterns. c1) XRD patterns of MFDFP containing different concentrations of heparin sodium. c2) XRD patterns of MFDFP containing different concentrations of mevastatin. d) Survey XPS spectrum. e–h) High-resolution XPS spectra of: e) C1s, f) N1s, g) S2p, and h) O1s.

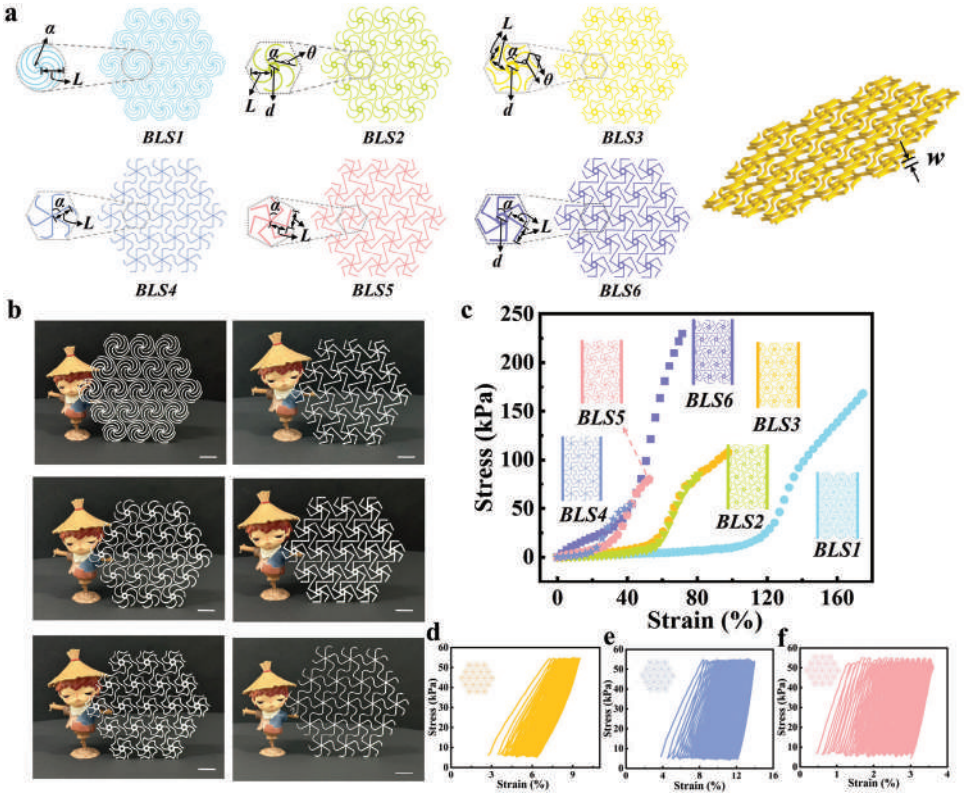

Figure 3. a) Structural design and geometric parameters of the six BLSs. b) BLS prepared by 4D printing. Scale bar = 20 mm. c) Stress–strain curves of BLSs under tensile loading. d–f) Stress–strain curves of d) BLS3, e) BLS4, and f) BLS5 under 500 cycles of tensile loading.

durability of the BLSs was analyzed, and the BLSs remained intact after 500 tensile test cycles, demonstrating excellent cyclic stability (Figure 3d–f). The cyclic loading and unloading curves of the BLSs showed hysteresis, which was an energy dissipation caused by internal friction. The energy dissipation was obvious at the beginning stage. With the increase in cycle times, the hysteresis gradually decreased, and the increment of residual strain also became smaller. In summary, the degree of ligament bending and nodes were the main determinants of the deformation behavior at different stages of BLSs. The greater degree of ligament bending and the introduction of nodes significantly increased the toughness of the structure, resulting in a greater proportion of the "bending-dominated" phase of the three-stage deformation process. Correspondingly, the critical deformation from "bending dominant" to "tensile dominant" also increased. Thus, the controllable regulation of the mechanical performance of metamaterial structures can be realized through the design of metamaterial structural parameters.

2.3. Design and Characterization of 4D Printed Personalized Occlusion Device

Based on the BLS, the disc structure of the occlusion device was designed. Since the left and right discs were the key influencing factors in determining the performance of the occlusion device, 4D printed shape memory VSD occlusion devices with different levels of disc structures were developed to achieve adjustability of the mechanical performance and further improve the sealing reliability. As shown in **Figure** 4a, the designed occlusion device contained one-, two-, or three-level disc structures. The occlusion devices with different biomimetic disc structures were named BLS1-OD, BLS2-OD, BLS3-OD, BLS4-OD, BLS5-OD, and BLS6-OD. The disc of the one-level occlusion device contained a single layer of biomimetic ligaments. Both the left and right discs of the two-level occlusion device contained two layers of biomimetic ligaments. On the one hand, the left and right discs were able to clamp the interventricular septum and improve the stability of the device. On the other hand, both the left and right sides contained two layers of biomimetic ligaments, and the blood flow blocking ability was enhanced. The three-level occlusion device contained three layers of biomimetic ligaments in each of the left and right discs, further enhancing stability, mechanical performance, and sealing reliability. After implanting the occlusion device, the blood flow within the ventricle causes pressure on the occlusion device, so the ability of different configurations of occlusion devices to withstand compressive loads was investigated (Figure 4b,c). It can be seen that the VSD occlusion devices with different configurations showed similar compression behavior, with the load-displacement curves first showing an "elastic zone" and then a large increase in slope to show a "dense zone." In general, under identical compression loads, the three-level occlusion device exhibited less deformation in comparison to the two-level occlusion device, indicating its superior capacity for load-bearing.

To simulate the deformation of the occlusion device during practical application, the VSD occluding conditions were

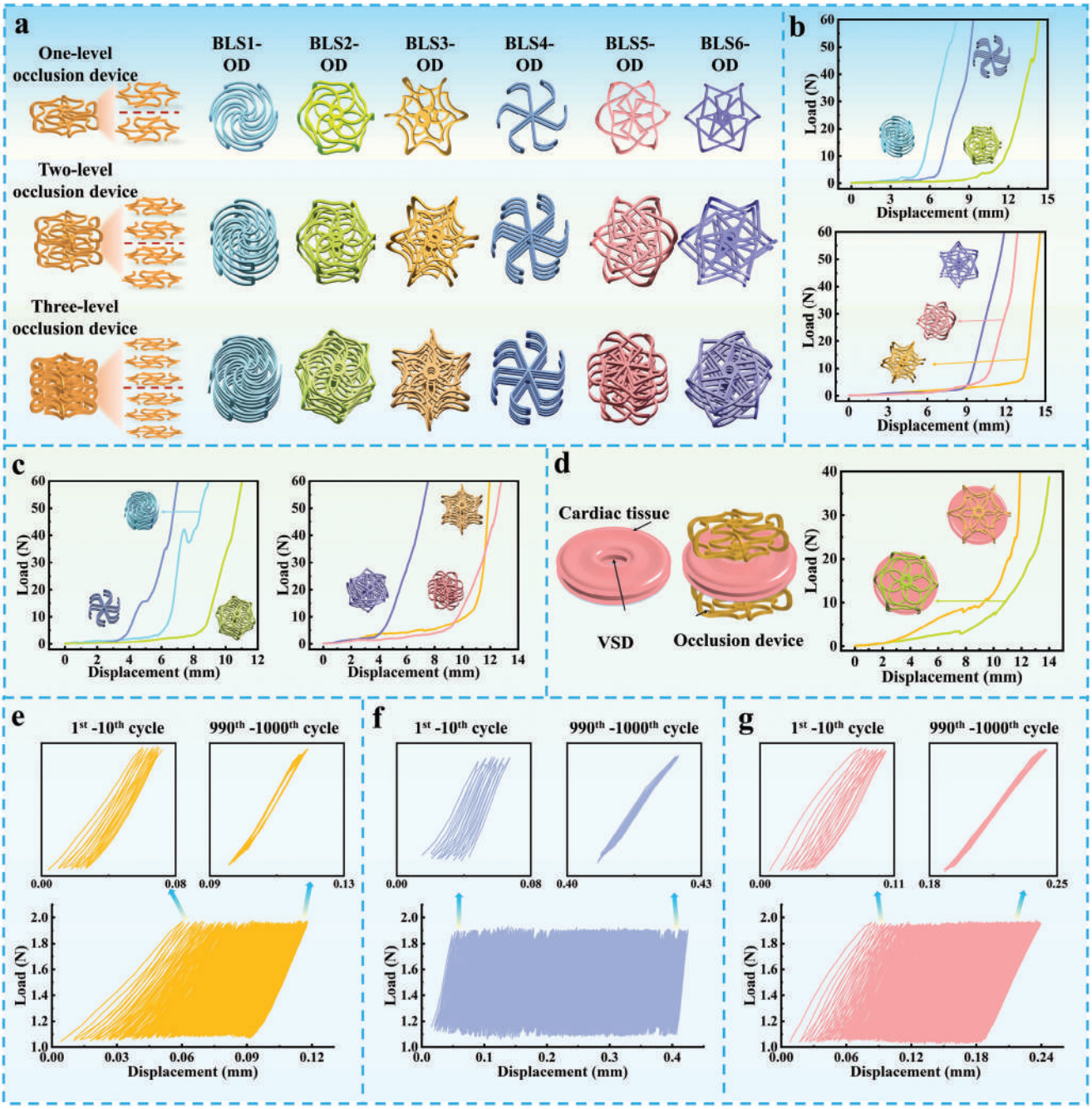

Figure 4. a) 4D printed cardiac occlusion devices with different hierarchical disc structures. b) Load-displacement curves of the two-level occlusion device. c) Load-displacement curves of the three-level occlusion device. d) Load-displacement curves of two-level occlusion devices with cardiac tissue. e–g) Load-displacement curves of e) BLS3-OD, f) BLS4-OD, and g) BLS5-OD subjected to 1000 cycles of compression.

simulated and compression loading was applied to both the occlusion device and the isolated porcine cardiac tissue. The cardiac tissue was modeled as a VSD structure with a 6-mm diameter hole in the middle. The left and right discs of the occlusion device were clamped on both sides of the hole, and then the compression load was applied. It can be seen that the compression behavior of the occlusion devices under the simulated occluding conditions also showed "J-shaped" curves (Figure 4d). Compared with Figure 4b, under the same compression load, the two-level BLS3-OD demonstrated a stronger capacity to withstand the compression load, preliminarily indicating the reliability of the occlusion device in the actual application process. Besides, to assess the durability of the device under compression loading, the 4D printed occlusion device was subjected to a 1000-cycle compression test (Figure 4e–g; and Figure S10, Supporting Information). In 1000 cycles of loading and unloading, the deformation of BLS3-OD was at a very low level compared to other BLS-ODs at the same load. BLS3-OD also demonstrated very weak hysteresis

in 990–1000 cycles, with good consistency in the cycling curves. This indicated that BLS3-OD had the most excellent energy dissipation capacity and deformation stability, demonstrating outstanding mechanical durability.[28]

2.4. Biocompatibility of 4D Printed Cardiac Occlusion Device

The occlusion device will play a role as a platform for cell and tissue adhesion/growth, therefore its biocompatibility is crucial. Cardiomyocytes and endothelial cells are important constituent cells of cardiac tissues, therefore, cardiomyocytes (H_9C_2) and human umbilical vein endothelial cells (HUVEC) were used to be cocultured with 0%MFDFP, 2%Hs/1%Me-MFDFP, 2%Hs/2%Me-MFDFP, and 2%Hs/4%Me-MFDFP, respectively. The cytocompatibility of MFDFP was evaluated using the Cell Counting Kit-8 (CCK-8) assay and Calcein AM/PI staining assay (**Figure 5a**). Both H_9C_2 and HUVEC demonstrated high cell viability after coculture, and the cell viability of H_9C_2 showed an increasing trend with the addition of mevastatin, which verified its efficacy in promoting cell proliferation (Figure 5b,c). The cell state was visualized by live-dead staining, and with the increase of coculture time, the cells significantly proliferated and remained in a highly active state, indicating the excellent cytocompatibility and highly efficient proproliferation effect of MFDFP (Figure 5d,e). In addition, the cell morphology of HUVEC in the 2%Hs/1%Me-MFDFP, 2%Hs/2%Me-MFDFP, and 2%Hs/4%Me-MFDFP groups was more aggregated than that of the control group, which may be attributed to the promotion of cell adhesion by mevastatin.

To further evaluate the biosafety of the 4D printed cardiac occlusion device, the occlusion device was implanted subcutaneously into Sprague–Dawley (SD) rats. All rats were able to eat, defecate, and exercise normally, with no infection or swelling at the implantation sites. Histological analysis of tissues adherent to the implanted occlusion device was performed. After implantation of the device, a series of host immune responses were triggered, which accelerated the integration of the device into surrounding tissues and promoted tissue growth. Two weeks after implantation of the occlusion device, inflammatory cells infiltrated, recruited into the surrounding tissue, and were less distinguishable from the surrounding border. Neoplastic capillaries were observed, suggesting that the occlusion device was able to promote tissue growth (**Figure 6a**). Four weeks after implantation, lax capsular structures of comparable thickness were observed, and there was a large number of inflammatory cells infiltrated, accompanied by a fibrous tissue layer on the inner side. The two-level occlusion device exhibited more lax capsular structures than the one-level occlusion device group, probably due to the two-level occlusion device containing more biomaterials that can initiate a stronger host immune response. In addition, the two-level occlusion device group contained more MFDFP, which was more conducive to promoting tissue growth (Figure 6a). Eight weeks after implantation, the capsule structure was tighter and tougher, while the fibroblast layer demonstrated a thin and dense state. Similarly, Masson staining revealed that there was considerable amount of collagen present in the tissue (Figure 6a), with the two-level occlusion device having higher collagen content than the one-level occlusion device. After implantation of the occlusion device, an inflammatory response occurred and the inflammatory signals stimulated fibroblast proliferation and tissue growth. Furthermore, no abnormalities were observed in tissue sections of the heart, liver, spleen, lungs, and kidneys following implantation of the occlusion device (Figure 6b; and Figures S16–S18, Supporting Information). Thus, the in vivo implantation experiments demonstrated that the 4D printed cardiac occlusion device had excellent biosafety and biocompatibility, and the two-level occlusion device group was more advantageous in promoting tissue growth compared to the one-level occlusion device group. Additionally, since the device was in contact with blood postimplantation, its hemocompatibility was evaluated. As illustrated in Figure S19 (Supporting Information), no obvious hemolysis was observed, and the hemolysis rate of MFDFP was all below 2.5%, thereby satisfying the safety criterion of a hemolysis rate under 5% and indicating excellent blood safety.[29]

2.5. Functional Verification of 4D Printed Cardiac Occlusion Device

The occlusion device provides a temporary bridge for autologous repair and guides cell and tissue growth, leading to endothelialization. Cell migration and proliferation are crucial for rapid encapsulation of the occlusion device and acceleration of the endothelialization process, therefore, the effect of MFDFP on the proliferation of HUVEC was examined using the EdU assay. As shown in **Figure 7a,b**, the proportion of EdU-positive cells in the 2%Hs/2%Me-MFDFP group and the 2%Hs/4%Me-MFDFP group gradually increased compared with that in the 0%MFDFP group. This indicated that mevastatin in MFDFP promoted the proliferation of HUVEC, and the promotion effect was more significant with the increase of mevastatin. In addition, wound healing assays were employed to detect the cell migration ability of HUVEC (Figure 7c). At 0 h, the groups demonstrated an almost uniform wound area. After 12 h, the wound area was significantly reduced. Compared to the 0%MFDFP group, the three drug-loaded MFDFP groups showed faster wound healing rates. The wound area gradually decreased with the increase of mevastatin concentration, and the 2%Hs/4%Me-MFDFP group demonstrated a significantly reduced wound area. Accordingly, the cell migration ratio of HUVEC was inversely proportional to the size of the wound area. At 24 h, the wound area continued to decrease and the migration rate continued to increase, reaching a maximum of nearly 80% in the 2%Hs/4%Me-MFDFP group (Figure 7d). In addition, endothelial differentiation markers CD31 and vWF were used to track the effect of the occlusion device on endothelialization. The significant increase in the number of CD31-positive cells and vWF-positive cells in the occlusion device was probably due to increased neovascularization, indicating a favorable endothelialization promotion effect (Figure 7e). The above results indicated that the occlusion device with MFDFP had an outstanding promotion effect on HUVEC proliferation and migration, and the promoting efficacy was more obvious with the increase of mevastatin content.

Thrombosis is one of the serious complications after implantation of an occlusion device, so efficient anticoagulation and prevention of thrombosis are necessary functions of the next-generation occlusion devices. Enhanced proliferation and

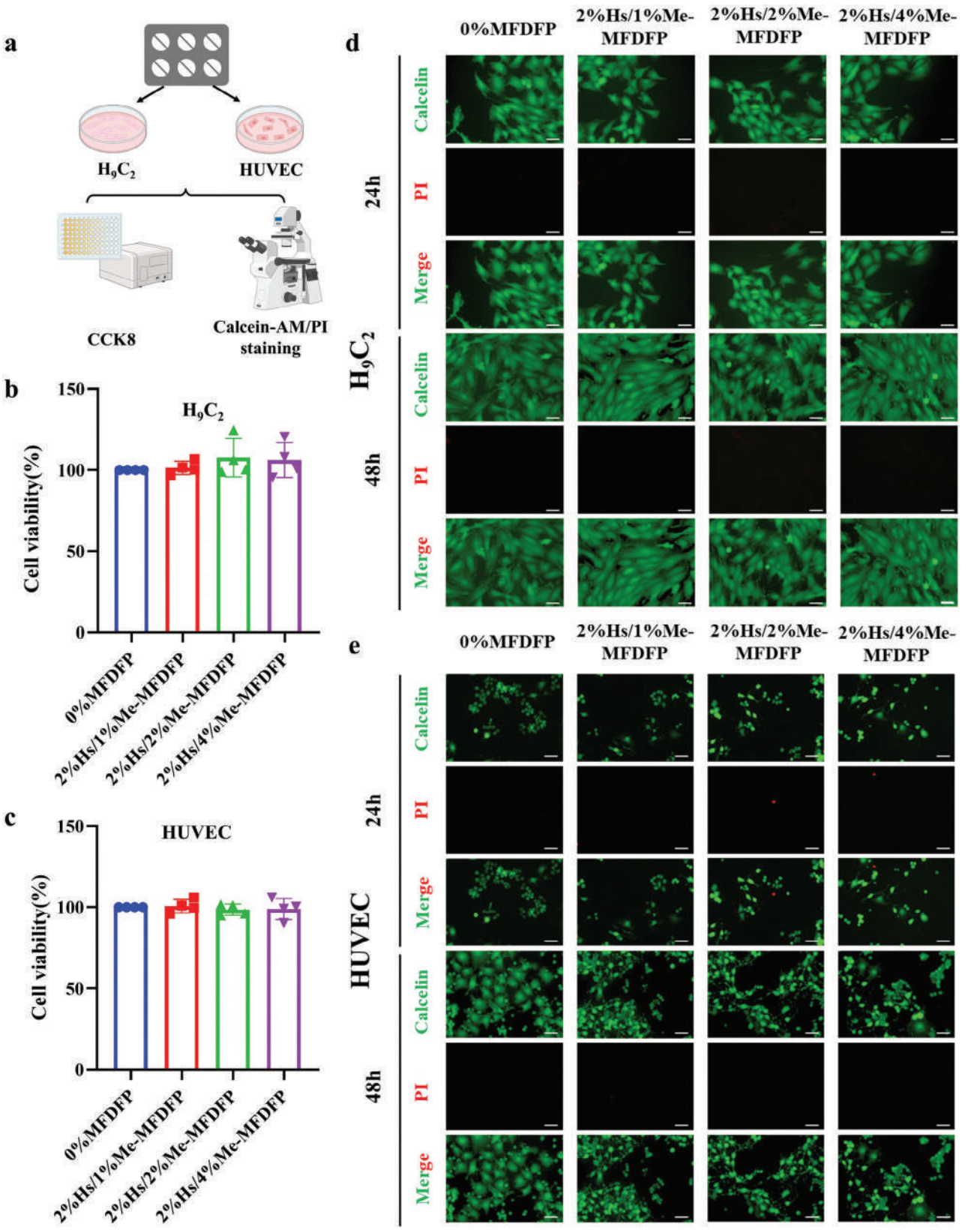

Figure 5. Cytocompatibility characterization of MFDFP. a) Schematic of the cytocompatibility assays. b) Cell viability of H_9C_2 cocultured with MFDFP for 48 h, $n = 4$. c) Cell viability of HUVEC cocultured with MFDFP for 48 h, $n = 4$. d) Live/dead staining images of H_9C_2 after coculture with MFDFP. Scale bar = 50 µm, $n = 3$. e) Live/dead staining images of HUVEC after coculture with MFDFP. Scale bar = 50 µm, $n = 3$.

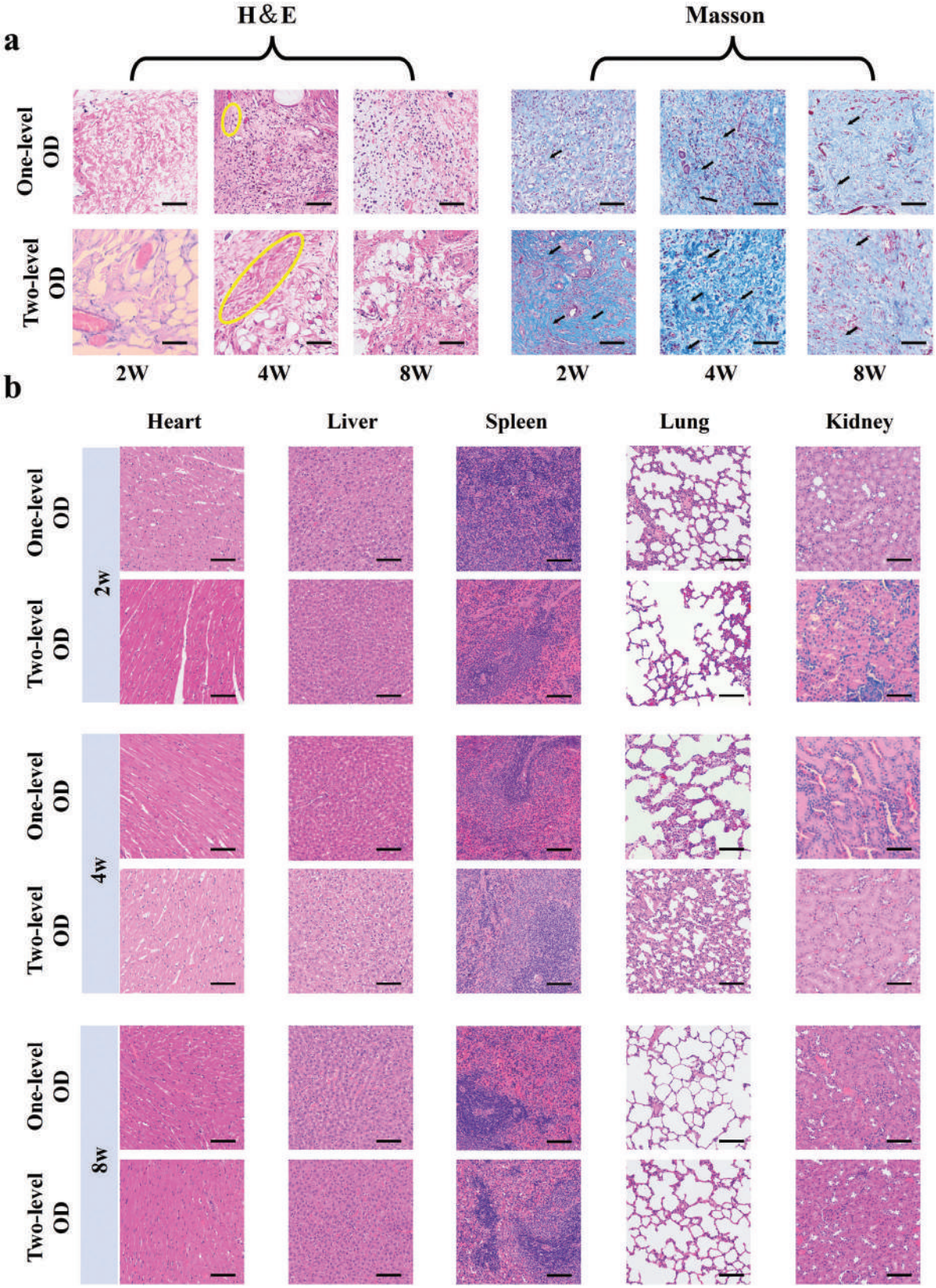

Figure 6. a) Histological analysis of tissues adjacent to the occlusion device. Yellow circles represent fibrous tissue, and the black arrows indicate collagen. 2w, 4w, and 8w represent 2, 4, and 4 weeks postimplantation, respectively. Scale bar = 100 μm. b) Histological analysis of major organs. Scale bar = 100 μm.

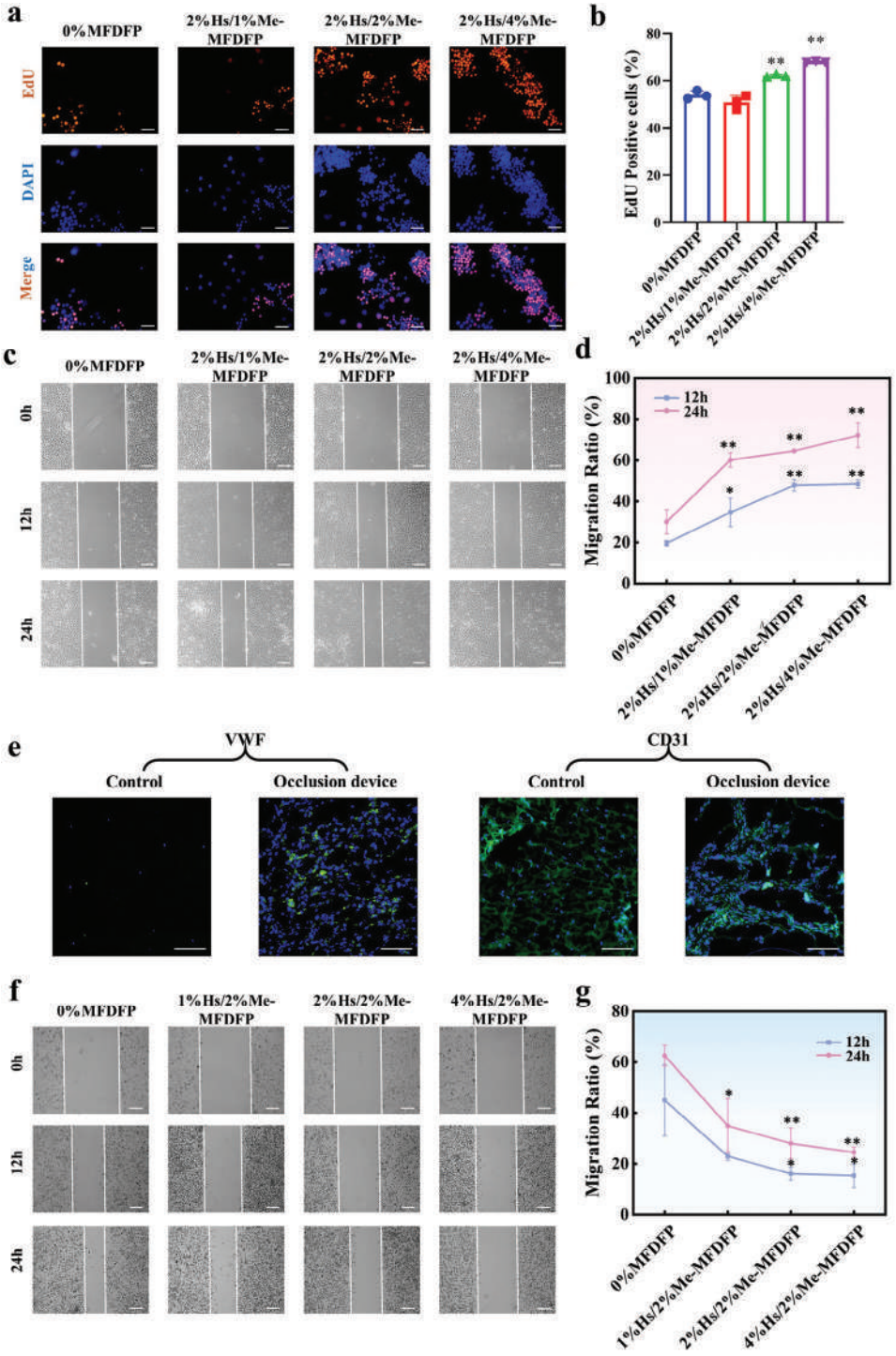

Figure 7. Functional validation of 4D printed cardiac occlusion device. a) EdU staining of HUVEC. Scale bar = 50 μm. b) Proportion of EdU-positive cells. $n = 3$, $P = 0.0018$ in 2%Hs/2%Me-MFDFP versus 0%MFDFP, *t*-test. $P = 0.0044$ in 2%Hs/4%Me-MFDFP versus 0%MFDFP, Wilcoxon test. Data are presented as mean ± SD. c) Wound healing assays of HUVEC after 12 and 24 h coculture with MFDFP. Scale bar = 200 μm. d) Migration ratios of HUVEC. $n = 3$, $P = 0.0212$ in 2%Hs/1%Me-MFDFP versus 0%MFDFP after 12 h, *t*-test. $P = 0.0016$ in 2%Hs/1%Me-MFDFP versus 0%MFDFP after 24 h, *t*-test. $P < 0.0001$ in 2%Hs/2%Me-MFDFP versus 0%MFDFP after 12 h, *t*-test. $P = 0.0091$ in 2%Hs/2%Me-MFDFP versus 0%MFDFP after 24 h, Wilcoxon test. $P < 0.0001$ in 2%Hs/4%Me-MFDFP versus 0%MFDFP after 12 h, *t*-test. $P = 0.0010$ in 2%Hs/4%Me-MFDFP versus 0%MFDFP after 24 h, *t*-test. Data are presented as mean ± SD. e) Immunofluorescence staining of adjacent tissues after implantation of the occlusion device in vivo. f) Wound healing assays of VSMC after 12 and 24 h coculture with MFDFP. Scale bar = 200 μm. g) Migration ratios of VSMC. $n = 3$, $P = 0.0138$ in 1%Hs/2%Me-MFDFP versus 0%MFDFP after 24 h, *t*-test. $P = 0.0245$ in 2%Hs/2%Me-MFDFP versus 0%MFDFP after 12 h, *t*-test. $P = 0.0012$ in 2%Hs/2%Me-MFDFP versus 0%MFDFP after 24 h, *t*-test. $P = 0.0253$ in 4%Hs/2%Me-MFDFP versus 0%MFDFP after 12 h, *t*-test. $P = 0.0001$ in 4%Hs/2%Me-MFDFP versus 0%MFDFP after 24 h, *t*-test. Data are presented as mean ± SD. $*p < 0.05$, $**p < 0.01$ versus 0%MFDFP.

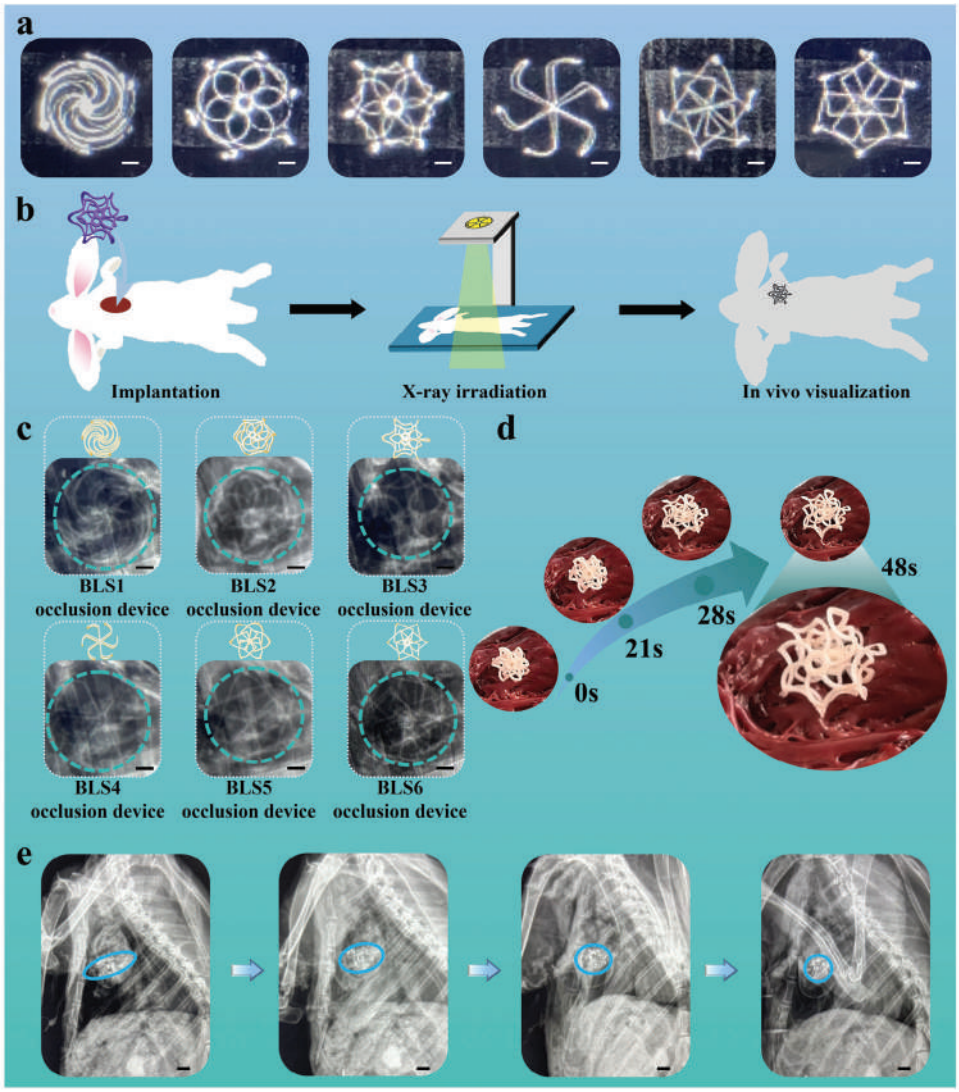

Figure 8. a) Evaluation of radiopacity of 4D printed occlusion device in vitro. b) Schematic of evaluating radiopacity of the occlusion devices implanted in rabbits. c) Evaluation of the radiopacity of the 4D printed occlusion device implanted in rabbits. d,e) The process of the 4D printed occlusion device sealing the VSD. d) Sealing VSD in the isolated porcine heart. e) Sealing VSD in the in vivo rabbit heart. Scale bar = 5 mm.

migration of vascular smooth muscle cells (VSMC) are important processes leading to thrombosis. Hence, the effects of MFDFP on VSMC migration and proliferation were analyzed by wound healing assays. Compared with the wound area at 0 h, the wound area in the 0%MFDFP group was significantly reduced after 12 h, while the wound area in the 2%Hs/2%Me-MFDFP and 4%Hs/2%Me-MFDFP groups showed less change (Figure 7f). Compared with the 0%MFDFP group, the 1%Hs/2%Me-MFDFP, 2%Hs/2%Me-MFDFP, and 4%Hs/2%Me-MFDFP groups exhibited reduced cell migration ratios (Figure 7g). At 24 h, the effect of MFDFP in inhibiting the migration of VSMC was more significant, and the wound area in the 4%Hs/2%Me-MFDFP group was almost unchanged. This indicated that heparin sodium inhibited the migration of VSMC, and the inhibition effect was stronger with the increase of heparin sodium content. Therefore, the inhibition of MFDFP on the proliferation and migration of VSMC validated the efficacy of MFDFP as a highly effective anticoagulant.

In addition, the radiopacity of the 4D printed occlusion device was evaluated using X-rays, and the configuration of the entire occlusion device structure was clearly visible under X-ray irradiation, demonstrating homogeneous visualization characteristics. Homogeneous visualization is crucial for precise positioning, as it can avoid complications such as displacement caused by improper positioning (**Figure** 8a–c). Besides, the programmable reconfigurability and sealing characteristics of the occlusion device were assessed (Figure 8d,e). The 4D printed shape memory VSD occlusion device was programmed under external stimulation into a linear temporary configuration with a small cross-sectional area that facilitated minimally invasive implantation. A VSD model was established on an isolated porcine heart and the linear occlusion device was implanted. The occlusion device discs were gradually deployed under thermal stimulation and

eventually reverted to the original dual-disc structure, demonstrating the dynamic reconfigurability of the VSD occlusion device. To further verify the reconfigurability and sealing feasibility of the occlusion device, an in vivo VSD model was established in the New Zealand rabbit, and the sealing process was monitored in real-time under X-ray. The occlusion device in a temporary configuration was delivered to the VSD site and thermal stimulation was applied by injecting physiological saline solution (41 °C) through a catheter. Under X-ray, the process of reconfigurable transformation was clearly observed, and the transformation process took less than 1 min, achieving adaptive deployment and sealing effectiveness. The influence of thermal stimulation on the cytocompatibility and cell function was analyzed. After being incubated at 41 °C for 60 s, both HUVEC and H_9C_2 still demonstrated remarkable cell viability, and HUVEC displayed outstanding proliferative capacity (Figure S22, Supporting Information).

3. Conclusion

In summary, a multifunctional fiber platform was innovatively designed to develop a novel next-generation bioabsorbable 4D printed shape memory cardiac occlusion device. The device realized personalized configuration, anticoagulation, endothelialization promotion, and precise localization, effectively addressing problems of current occlusion devices, such as thrombosis, slow endothelialization, and abrasion. The combination of biomimetic ligament-based disc structure and multilevel configuration endowed the device structure with high design freedom, which provided a guarantee for customizing the mechanical performance of the device. Besides, it helped to achieve synergistic deformation with myocardial tissues, reducing the risk of abrasion. Wound healing assays verified the excellent pro-HUVEC and anti-VSMC proliferation/migration ability of MFDFP, contributing to efficient anticoagulation and accelerated endothelialization. Under X-rays, the occlusion device achieved homogenous visualization in vivo, which facilitated precise localization. Histological analysis of the adhesive tissues of the device and analysis of endothelial differentiation markers CD31 and vWF demonstrated that the 4D printed occlusion device was outstandingly biocompatible and capable of promoting endothelialization. The occlusion device is expected to be an effective next-generation device for personalized treatment of cardiac defects, laying a solid foundation and pointing the direction for the future development of occlusion devices.

4. Experimental Section

Preparation of MFDFP: 1.045 g PCL (M_n = ≈60 000–65 000, Bide Pharmatech Ltd, China) and 0.055 g PEG (M_n = 400, Shanghai Aladdin Biochemical Technology Co., Ltd.) were dissolved in 9.9 g DCM (AR, Tianjin Fuyu Fine Chemical Co., Ltd.) and stirred for 5 h at 25 °C to obtain PEG/PCL solution. Then, Mevastatin (1 wt%, 2 wt%, 4 wt%, HPLC, Shanghai Macklin Biochemical Technology Co., Ltd.) was added and stirred for another 5 h to obtain a uniform composite solution. Heparin sodium (1 wt%, 2 wt%, 4 wt%, 185 USP units mg^{-1}, Shanghai Macklin Biochemical Technology Co., Ltd.) was dissolved in deionized water (DI water) to obtain an ultrasonic spray solution. The electrospinning solution was pipetted into a syringe and the air bubbles were exhausted, then the syringe was connected to a microsyringe pump for spinning. The parameters of electrospinning were as follows: The needle diameter was 0.25 mm, the voltage was 20 kV, the injection flow rate was 120 μL min^{-1}, the distance between the receiving drum and the syringe was 15 cm, and the rotating speed of the drum was 300 rpm. Electrospinning was carried out at room temperature, and the white fiber film was collected on the receiving drum. Then, the prepared heparin sodium ultrasonic spray solution was transferred to the syringe, and the solution was evenly sprayed on the surface of the fiber film by the ultrasonic spray machine. After 1 h, the MFDFP was prepared.

Fabrication of 4D Printed Radiopaque Composite Filaments: $BaSO_4$-PEG/PLA 4D printing filaments were prepared using a twin-screw extruder with a mass ratio of 2.5: 19.5: 78. The uniformly mixed $BaSO_4$, PEG, and PLA were loaded into the feed hopper and successively passed through 9 consecutive heating chambers for melt extrusion, with a temperature range of 170–200 °C. The extruder speed was set at 50 rpm, and the die diameter was 1.75 mm.

Preparation of 4D Printed Cardiac Occlusion Device: The device was modeled using Siemens PLM Software UG NX 1953 software and the STL format file was exported. The STL file was imported into Ultimaker Cura slicing software, and the printing speed, nozzle temperature, and printing platform temperature were set to 20 mm s^{-1}, 190, and 40 °C, respectively. Then, the 3D model was sliced, and the print path was automatically generated to get a slice file in Gcode format. The slice file was imported into a fused deposition 3D printer (TENLOG HANDS2) for printing.

FTIR Tests: MFDFP samples of size 10 mm × 10 mm were prepared and analyzed for chemical functional groups using FTIR spectroscopy (Nicolet iS50, Thermo-Fisher Scientific). The scanning range was 4000–400 cm^{-1}.

XRD Tests: MFDFP samples of 10 mm × 10 mm size were prepared to analyze the crystalline properties of MFDFP using an X-ray diffractometer (Bruker, Germany). The samples were scanned in the range of 5°–90° at 10° min^{-1} to obtain the diffraction peak data. The data were analyzed using MDI Jade 6.5 software to obtain the diffraction pattern of MFDFP.

XPS Tests: A 10 mm × 10 mm MFDFP sample was prepared to characterize the elemental composition of MFDFP using X-ray photoelectron spectroscopy (Thermo Scientific K-Alpha). The data were imported into Avantage software for XPS spectral analysis, and the element composition and content of each element were analyzed according to the peak location and peak area. The photoelectron and ohmic electron energy distributions were obtained by irradiating the sample surface using X-ray photons, and then the distribution of elements in the MFDFP sample was analyzed.

Mechanical Performance: Uniaxial tensile was performed using a Zwick 010 tester. The MFDFP was prepared as a 10 mm × 70 mm strip sample. The upper and lower ends of the sample in contact with the fixture were wrapped with tape to increase the thickness, avoiding the sample falling off during loading. The testXpert software was used to control the test conditions, the preload was set to 0.05 N, and the test speed was 10 mm min^{-1} in displacement-controlled mode. The printed BLSs were tested at 37 °C by Zwick 010 for uniaxial tensile test. The preload for the test was 0.15 N and the loading speed was 10 mm min^{-1}.

The compression performance analysis of the 4D printed occlusion device was performed using a Zwick 010 tester. The tests included uniaxial compression tests, cyclic compression tests, and simulated occluding compression tests. The occlusion device was placed between the compression fixtures and the loading speed was set at 2 mm min^{-1}. In the cyclic test, the maximum and minimum loads for cyclic compression were set to 1 N and 2 N, respectively, and the number of cycles was set to 1000. In addition, a 30 mm-diameter circular sample of isolated porcine heart tissue was prepared and a 6 mm-diameter VSD model was fabricated. The porcine cardiac tissue was then placed between the double discs of the occlusion device to simulate the deformation behavior of the occlusion device subjected to compressive loading at the VSD site. The test was performed at a loading speed of 2 mm min^{-1}.

CCK-8 and Live-Dead Staining Assays: The 0%MFDFP, 2%Hs/1%Me-MFDFP, 2%Hs/2%Me-MFDFP, and 2%Hs/4%Me-MFDFP samples (5 mm × 5 mm) were thoroughly sterilized using UV light. H_9C_2 and HUVEC were inoculated into 96-well plates containing 0%MFDFP, 2%Hs/1%Me-MFDFP, 2%Hs/2%Me-MFDFP, and 2%Hs/4%Me-MFDFP samples, and

cocultured for 24 and 48 h in a humidified atmosphere containing 5% CO_2 at 37 °C. After coculture, the medium was discarded and the cells were gently rinsed with PBS. Cells were incubated with premix containing CCK-8 (SC119, SEVEN BIO, China) for 30 min in a dark cell incubator. When the color of the liquid in the wells changed significantly, the absorbance was measured at 450 nm. In addition, a live-dead staining assay was performed. 1 mL of Calcein AM/PI (Invitrogen) staining solution was added and incubated at 37 °C in the dark for an additional 30 min. Fluorescent images of each group of live/dead cells were taken in a dark room (AxioCam MRc 5, Carl Zeiss, Germany).

Wound Healing Assays: Prior to seeding the cells, three parallel lines were marked on the bottom of the capsule at 0.5 cm intervals for precise localization. HUVEC and VSMC were cocultured with MFDFP samples (5 mm × 5 mm) of different drug loading concentrations. Once the cell density reached 100%, a scratch perpendicular to the bottom parallel line was generated using a 200 μL pipette tip. Subsequently, the medium was discarded and rinsed three times with PBS to eliminate any cellular debris. Excess PBS was aspirated from the well plates and serum-free DMEM was added as fresh medium. The wound area was imaged after 0, 12, and 24 h using a Zeiss fluorescence microscope (AxioCam MRc 5, Carl Zeiss, Germany).

In Vivo Implantation Experiments: All in vivo experiments were performed according to the animal protection agency guidelines and approved by the Ethics Committee of the Harbin Medical University. Subcutaneous implantation was used to evaluate the histocompatibility and proendothelial efficacy of the occlusion device. BLS3 occlusion devices (2%Hs/2%Me-MFDFP) were selected for in vivo experiments due to their excellent strength, toughness, and mechanical stability. Sterilized occlusion devices were implanted into the back of anesthetized SD male rats. After 2, 4, and 8 weeks of implantation ($n = 3$), SD rats were euthanized and tissues adhering around the occlusion device were removed for histological analysis. The tissues were fixed by immersion in glutaraldehyde overnight and embedded in paraffin for tissue sectioning. Hematoxylin and eosin (H&E) and Masson staining were performed on tissues adjacent to the device to analyze the host response after implantation. Similar procedures were executed to perform histological analysis on the organs (heart, liver, spleen, lungs, kidneys) of SD rats. In addition, endothelial cells were stained using rabbit anti-CD31 antibody (1:500 dilution) and vWF antibody (1:500 dilution), and micrographs were taken under a fluorescent inverted microscope.

Radiopacity Characterization: X-ray examinations were conducted in dedicated rooms with safety partitions to isolate X-ray radiation. The 4D printed structure was placed on a platform, perpendicular to the detector probe, and the detection system was activated for imaging. A sterilized occlusion device was implanted near the heart of an anesthetized New Zealand White rabbit, and the wound was sutured and sterilized postimplantation. The rabbit was placed on the platform, the detector perpendicular to the platform was activated for examination, and in vivo imaging pictures were obtained. After imaging, the device was removed.

Programmable Reconfigurability: The transition temperature of 4D printed composites was 41 °C (Figure S20, Supporting Information). The 4D printed structures were placed in a heated temperature chamber and elevated from room temperature at a rate of 5 °C min^{-1} to above the transformation temperature, followed by maintaining the temperature for 5 min. At this stage, as the 4D printed structure entered into a rubbery state, an external force was applied to induce deformation of the structure into the desired temporary configuration. The external force was kept constant, and the 4D printed structure was quickly removed from the temperature chamber and rapidly cooled to room temperature. The structure entered the glassy state, and its temporary configuration was fixed. By reheating the structure above its transition temperature, the structure underwent active deformation back to its original configuration, thereby enabling dynamic transformation and shape recovery process. Usually, the programmable reconfigurability or the shape recovery property is measured by the shape recovery rate (R_r, Figure S21 and Formula S1, Supporting Information). The wing structures were printed to evaluate the programmable reconfigurability, as shown in Figure S23 (Supporting Information), with the R_r values of the two structures reaching 97.58% and 98.18%, respectively. Similarly, the 4D printed cardiac occlusion device was programmed to a temporary configuration with a smaller cross-sectional area. A hole-like VSD defect was created in the septal tissue of an isolated porcine heart, and the occlusion device in the temporary configuration was placed in the septal defect. The occlusion device was heated and the device reverted to the large-diameter disc configuration, with the disc diameter being ≈160% of that in the temporary configuration. The R_r of occlusion device reached up to 98.30%, which realized the effective sealing of the ventricular septal defect.

A VSD model was established on anesthetized New Zealand rabbits using Brokenbrough needles for puncture, and a balloon was inflated three times to create a VSD with a diameter of ≈6 mm. The BLS3 occlusion device was shaped into a temporary configuration was delivered to the VSD site via a catheter. A physiological saline solution at 41 °C was injected through a catheter, and the reconfigurable transformation of the occlusion device was observed in real-time under X-ray monitoring.

Statistical Analysis: The results were statistically analyzed by SPSS 26.0. All experiments were repeated three or more times. The Fisher test was applied to the distribution of data normality, and data in accordance with normal distribution were expressed as mean ± SD. The *t*-test was applied to the normally distributed data between the two groups, and the Wilcoxon test was applied to the non-normal group. The difference between groups was considered as statistical significance when $P < 0.05$.

Supporting Information

Supporting Information is available from the Wiley Online Library or from the author.

Acknowledgements

M.Y. and X.Y. contributed equally to this work. This work was funded by the National Key R&D Program of China (No. 2022YFB3805700), the Key R&D Program of Ningbo City (No. 2023Z191), the National Natural Science Foundation of China (No. 12302198), Heilongjiang Provincial Natural Science Foundation of China (No. LH2022A013), and Key Project of Heilongjiang Provincial Department of Science and Technology (No. 2022ZX02C25).

Conflict of Interest

The authors declare no conflict of interest.

Data Availability Statement

The data that support the findings of this study are available from the corresponding author upon reasonable request.

Keywords

4D printing, biomimetic structure, congenital heart defect, occlusion device, shape memory polymer

Received: July 15, 2024
Revised: November 1, 2024
Published online:

[1] P. Kong, X. Liu, Z. Li, J. Wang, R. Gao, S. Feng, H. Li, F. Zhang, Z. Feng, P. Huang, S. Wang, D. Zhuang, W. Ouyang, W. Wang, X. Pan, *Adv. Sci.* **2024**, *11*, 2305967.

[2] G. Guo, J. Hu, F. Wang, D. Fu, R. Luo, F. Zhang, C. Hu, J. Chen, X. Pan, L. Yang, Y. Wang, X. Zhang, *Biomaterials.* **2022**, *291*, 121909.
[3] C. Lin, L. Liu, Y. Liu, J. Leng, *Acta Biomater.* **2021**, *128*, 100.
[4] Z. Zhang, Y. Xiong, J. Hu, X. Guo, X. Xu, J. Chen, Y. Wang, Y. Chen, *J. Funct. Biomater.* **2022**, *13*, 182.
[5] Z. Xiang, J. Zhang, C. Zhou, B. Zhang, N. Chen, M. Li, D. Fu, Y. Wang, *ACS Appl. Mater. Interfaces.* **2023**, *15*, 42341.
[6] Y. Huang, Y. S. Wong, H. C. A. Ng, F. Y. C. Boey, S. Venkatraman, *Bioeng. Transl. Med.* **2017**, *2*, 156.
[7] Z. Meng, X. Mu, J. He, J. Zhang, R. Ling, D. Li, *Int. J. Extreme Manuf.* **2023**, *5*, 025001.
[8] J. Song, B. Lv, W. Chen, P. Ding, Y. He, *Int. J. Extreme Manuf.* **2023**, *5*, 032008.
[9] H. Budharaju, D. Sundaramurthi, S. Sethuraman, *Bioact. Mater.* **2024**, *32*, 356.
[10] B. Jian, H. Li, X. He, R. Wang, H. Y. Yang, Q. Ge, *Int. J. Extreme Manuf.* **2024**, *6*, 012001.
[11] C. Qin, C. Wu, *VIEW.* **2022**, *3*, 20210018.
[12] E. Yarali, M. J. Mirzaali, A. Ghalayaniesfahani, A. Accardo, P. J. Diaz-Payno, A. A. Zadpoor, *Adv. Mater.* **2024**, *36*, 2402301.
[13] M. Chen, M. Gao, L. Bai, H. Zheng, H. J. Qi, K. Zhou, *Adv. Mater.* **2023**, *35*, 2209566.
[14] X. Wan, Z. Xiao, Y. Tian, M. Chen, F. Liu, D. Wang, Y. Liu, P. Bartolo, C. Yan, Y. Shi, R. R. Zhao, H. J. Qi, K. Zhou, *Adv. Mater.* **2024**, 2312263.
[15] D. B. Mahmoud, M. Schulz-Siegmund, *Adv. Healthcare Mater.* **2023**, *12*, 2202631.
[16] Y. Zhang, A. Raza, Y. Xue, G. Yang, U. Hayat, J. Yu, C. Liu, H. Wang, J. Wang, *Bioact. Mater.* **2023**, *23*, 343.
[17] A. A. Alsharif, J. M. Aviles, F. M. Zechel, N. A. Alsharif, N. El-Atab, *VIEW.* **2024**, *5*, 2024008.
[18] J. Lai, Y. Liu, G. Lu, P. Yung, X. Wang, R. S. Tuan, Z. A. Li, *Bioact. Mater.* **2024**, *37*, 348.
[19] Y. Deng, B. Yang, F. Zhang, Y. Liu, J. Sun, S. Zhang, Y. Zhao, H. Yuan, J. Leng, *Biomaterials.* **2022**, *291*, 121886.
[20] A. Chen, J. Su, Y. Li, H. Zhang, Y. Shi, C. Yan, J. Lu, *Int. J. Extreme Manuf.* **2023**, *5*, 032007.
[21] D. Wang, L. Dong, G. Gu, *Adv. Funct. Mater.* **2023**, *33*, 202208849.
[22] J. Zhou, J. Chang, X. Song, Z. Li, L. Zhang, H. Li, J. Zhang, D. Yan, C. Zhang, *Composites, Part B.* **2024**, *275*, 111284.
[23] L. Mungenast, R. Nieminen, C. Gaiser, A. B. Faia-Torres, J. Rühe, L. Suter-Dick, *Biomater. Biosyst.* **2023**, *11*, 100081.
[24] J. Zhang, X. Zha, G. Liu, H. Zhao, X. Liu, L. Zha, *Mater. Horiz.* **2024**, *11*, 1944.
[25] A. Rezaei, A. Khanzadeh, H. Behniafar, *J. Polym. Res.* **2023**, *30*, 91.
[26] D. Yan, J. Chang, H. Zhang, J. Liu, H. Song, Z. Xue, F. Zhang, Y. Zhang, *Nat. Commun.* **2020**, *11*, 1180.
[27] X. Xin, L. Liu, Y. Liu, J. Leng, *Adv. Funct. Mater.* **2020**, *30*, 2004226.
[28] H. He, T. Yang, T. Liu, Y. Gao, Z. Zhang, Z. Yang, F. Liang, *Adv. Mater.* **2024**, *36*, 2312278.
[29] X. Chen, T. Yu, Q. Kong, H. Xu, Z. Zhao, G. Li, H. Fan, Y. Wang, *J. Mater. Chem. B.* **2023**, *11*, 2663.